### Observational study of hydrocarbons in the bright photodissociation region of Messier 8

M. Tiwari<sup>1,\*,</sup>, K. M. Menten<sup>1</sup>, F. Wyrowski<sup>1</sup>, J.P. Pérez-Beaupuits<sup>2,1</sup>, M.-Y. Lee<sup>1</sup>, W.-J. Kim<sup>3,1</sup>

- Max-Planck Institute for Radioastronomy, Auf dem Hügel, 53121 e-mail: mtiwari@mpifr.mpg.de
- European Southern Observatory, Alonso de Córdova 3107, Vitacura Casilla 7630355, Santiago, Chile
- Instituto de Radioastronomía Milimétrica, Avenida Divina Pastora 7, 18012 Granada, Spain

#### **ABSTRACT**

Aims. Hydrocarbons are ubiquitous in the interstellar medium, but their formation is still not well understood, depending on the physical environment they are found in. Messier 8 (M8) is host to one of the brightest HII regions and photodissociation regions (PDRs) in our galaxy. With the observed  $C_2H$  and  $c-C_3H_2$  data toward M8, we aim at obtaining their densities and abundances and to

Methods. Using the Atacama Pathfinder Experiment (APEX) 12 m, and the Institut de Radioastronomie Millimétrique (IRAM) 30 m telescopes, we performed a line survey toward Herschel 36 (Her 36), which is the main ionizing stellar system in M8, and an imaging survey within  $1.3 \times 1.3$  pc around Her 36 of various transitions of  $C_2H$  and  $C_3H_2$ . We used both Local Thermodynamic Equilibrium (LTE) and non-LTE methods to determine the physical conditions of the emitting gas along with the column densities and abundances of the observed species, which we compared with (updated) gas phase photochemical PDR models. In order to examine the role of polycyclic aromatic hydrocarbons (PAHs) in the formation of small hydrocarbons and to investigate their association with the HII region, the PDR and the molecular cloud, we compared archival Galactic Legacy Infrared Mid-Plane Survey Extraordinaire (GLIMPSE) 8  $\mu$ m and the Spectral and Photometric Imaging Receiver (SPIRE) 250  $\mu$ m continuum images with the C<sub>2</sub>H emission

Results. We observed a total of three rotational transitions of C<sub>2</sub>H with their hyperfine structure components and four rotational transitions of C<sub>3</sub>H<sub>2</sub> with ortho and para symmetries toward the H<sub>II</sub> region and the PDR of M8. Fragmentation of PAHs seems less likely to contribute to the formation of small hydrocarbons as the 8  $\mu$ m emission does not follow the distribution of C<sub>2</sub>H emission, which is more associated with the molecular cloud toward the north-west of Her 36. From the quantitative analysis, we obtained abundances of  $\sim 10^{-8}$  and  $10^{-9}$  for  $C_2H$  and c- $C_3H_2$  respectively, and volume densities of the hydrocarbon emitting gas in the range

Conclusions. The observed column densities of C<sub>2</sub>H and c-C<sub>3</sub>H<sub>2</sub> are reproduced reasonably well by our PDR models. This supports the idea that in high-UV flux PDRs, gas phase chemistry is sufficient to explain hydrocarbon abundances.

Buropean Southern Observatory, Alonso de Cordova 3107, Vitac 3 Instituto de Radioastronomía Milimétrica, Avenida Divina Pasto Received September ....; accepted ...

Aims. Hydrocarbons are ubiquitous in the interstellar medium, be physical environment they are found in. Messier 8 (M8) is host (PDRs) in our galaxy. With the observed C<sub>2</sub>H and c-C<sub>3</sub>H<sub>2</sub> data tow shed some light on their formation mechanism.

Methods. Using the Atacama Pathfinder Experiment (APEX) 12 n telescopes, we performed a line survey toward Herschel 36 (Her 36 survey within 1.3 × 1.3 pc around Her 36 of various transitions of (LTE) and non-LTE methods to determine the physical conditions of the observed species, which we compared with (updated) gas of polycyclic aromatic hydrocarbons (PAHs) in the formation of Hπ region, the PDR and the molecular cloud, we compared are (GLIMPSE) 8 μm and the Spectral and Photometric Imaging Recmaps.

Results. We observed a total of three rotational transitions of C transitions of C<sub>3</sub>H<sub>2</sub> with ortho and para symmetries toward the H likely to contribute to the formation of small hydrocarbons as the which is more associated with the molecular cloud toward the nabundances of ~ 10<sup>-8</sup> and 10<sup>-9</sup> for C<sub>2</sub>H and c-C<sub>3</sub>H<sub>2</sub> respectively, n(H<sub>2</sub>) ~ 5 × 10<sup>4</sup>-5 × 10<sup>6</sup> cm<sup>-3</sup>.

Conclusions. The observed column densities of C<sub>2</sub>H and c-C<sub>3</sub>H<sub>2</sub> is the idea that in high-UV flux PDRs, gas phase chemistry is sufficiently the idea that in high-UV flux PDRs, gas phase chemistry is sufficiently by the strong UV radiations from nearby bright stars, while PDRs are at the interface of these Hπ regions and cold molecular clouds shielded from the illuminating star (Tielens & Hollenbach 1985). In PDRs, the heating is regulated by FUV photons which give rise to a rich hydrocarbon chemistry (eg. Pety et al. 2005). Several studies on small hydrocarbons such as C<sub>2</sub>H and C<sub>3</sub>H<sub>2</sub> have been done in diffuse clouds (Lucas & Liszt 2000: 2005). Several studies on small hydrocarbons such as C<sub>2</sub>H and C<sub>3</sub>H<sub>2</sub> have been done in diffuse clouds (Lucas & Liszt 2000; Gerin et al. 2011), massive star-forming regions (Beuther et al. 2008), planetary nebulae (Schmidt & Ziurys 2017), dark clouds (Pratap et al. 1997), and PDRs (Teyssier et al. 2004; Pety et al. 2005; Cuadrado et al. 2015; Nagy et al. 2015). These hydrocarbons play a key role in understanding the carbon chemistry

taking place in both the gas phase and on grain surfaces. Several chemical pathways have been proposed for the formation of these hydrocarbons. It was found that in PDRs with low UV-flux ( $G_0 < 100$  in units of the Habing (1969) radiation field, where  $G_0 = 1$  corresponds to a flux of  $1.6 \times 10^{-3}$  erg cm<sup>-2</sup> s<sup>-1</sup> for FUV photons) such as the Horsehead nebula, the observed abundances of hydrocarbons were found to be higher than those predicted by gas-phase chemical PDR models by an order of magnitude (Teyssier et al. 2004). This suggested that the current gas-phase chemistry does not adequately explain the observed high abundances of hydrocarbons, which led to the proposition that additional mechanisms may be responsible for their production. Le Page et al. (2003), Pety et al. (2005) and Montillaud et al. (2013) suggest that one such mechanism is the fragmentation of polycyclic aromatic hydrocarbons (PAHs) due to far-UV radiation. While, in PDRs with a high UV-flux ( $G_0 \sim 10^4 - 10^5$  in Habing units) such as the Orion bar, the observed hydrocarbon abundances can be roughly explained by gas-phase chemistry. The molecular gas gets heated to higher temperatures in high UV flux PDRs facilitating new gas-phase formation routes, namely

Member of the International Max Planck Research School (IM-PRS) for Astronomy and Astrophysics at the Universities of Bonn and Cologne.

endothermic reactions, and reactions with activation energy barriers (Cuadrado et al. 2015).

Messier 8 (M8) is among the highest UV-flux ( $G_0 \sim 10^5$  in Habing units) (Tiwari et al. 2018) PDRs in the Milky Way. It is located in the Sagittarius-Carina arm, near our line of sight toward the Galactic Center. Its distance from the sun has been estimated as  $\sim 1.3$  kpc, a value we adopt (Damiani et al. 2004; Arias et al. 2006); see the discussion in Tothill et al. (2008). The open young stellar cluster NGC6530, the HII region NGC6523/33, and large quantities of molecular gas are associated with M8 (Tothill et al. 2008). The brightest star in the open cluster NGC6530 is Herschel 36 (Her 36) at R.A. ( $\alpha$ , J2000) =  $18^h03^m40^s$ .3 and Dec. ( $\delta$ , J2000) =  $-24^\circ22'43''$  (Woolf 1961), which has three main resolved components: a close massive binary consisting of an O9 V and a B0.5 V star and a more distant companion O7.5 star (Arias et al. 2010 and Sanchez-Bermudez et al. 2014).

An extensive survey of M8 at submillimeter, millimeter and far-infrared wavelengths was reported in Tiwari et al. (2018), where we explored in detail the morphology of the area around Her 36 and determined the physical conditions governing this region. Observations were performed using several receivers of the Stratospheric Observatory for Infrared Astronomy (SOFIA, Young et al. 2012), the Atacama Pathfinder EXperiment (APEX 12 m, Güsten et al. 2006) and the Institut de Radioastronomie Millimétrique (IRAM) 30 m telescopes. M8 has a face-on geometry, where the cold dense molecular cloud lies in the background with Her 36 being still very close to the dense core of the cloud from which it originated. Her 36 is fueling the HII region toward the east of it along with 9 Sagitarii (9 Sgr) (another binary with an O3.5 V and an O5-5.5V stars, Rauw et al. 2012) and a foreground veil of warm PDR gas is receding away from Her 36 toward the observer (see the sketch in Fig. 15 of Tiwari et al. 2018). Using various CO transitions from  $J = 1 \rightarrow$ 0 to 16  $\rightarrow$  15 at angular resolutions of  $\sim$  10" (minimum) for CO  $J = 6 \rightarrow 5$  to 30" (maximum) for CO  $J = 2 \rightarrow 1$  (Tiwari et al. 2018, Table 1), we determined the average kinetic temperatures in the region ranging from 100–150 K and the H<sub>2</sub> densities ranging from  $10^4$ – $10^6$  cm<sup>-3</sup>, with an H<sub>2</sub> column density of  $N(H_2) \sim$  $3.8 \times 10^{22} \text{ cm}^{-2}$ .

Several studies have addressed M8 in the X-ray, optical and IR regimes (Stecklum et al. 1995; Damiani et al. 2004; Arias et al. 2006; Goto et al. 2006; Damiani et al. 2017). Interestingly, Dahlstrom et al. (2013) found anomalously broad diffuse interstellar bands (DIBs) at 5780.5, 5797.1, 6196.0 and 6613.6 Å along with CH<sup>+</sup> and CH in absorption along the line of sight to Her 36. A bright IR source Her 36 SE (Goto et al. 2006) lying 0.25" south-east of Her 36, is responsible for radiative excitation of CH<sup>+</sup> and CH. The broadening of DIBs has been attributed to radiative pumping of closely spaced high-*J* rotational levels of small polar molecules (Dahlstrom et al. 2013; Oka et al. 2014; York et al. 2014).

With the goal to constrain the physical conditions of the gas responsible for the emission of small hydrocarbons and to verify if gas phase chemistry alone can explain the observed abundance of small hydrocarbons in M8, we here present an inventory of small hydrocarbons found toward M8 in a comprehensive survey including both observations toward the bright stellar system Her 36 and On-The-Fly (OTF) maps in a region of  $4' \times 4'$  (corresponding to  $1.5 \times 1.5$  pc) around Her 36 at millimeter- and submillimeter wavelengths. The organization of the paper is as follows. In Sect. 2, we summarize the observations done using

the PI230 and FLASH<sup>+</sup> receivers of the APEX<sup>1</sup> 12 m telescope and the EMIR receiver of the IRAM<sup>2</sup> 30m telescope. In Sect. 3, we present the spectra and the velocity integrated maps of the observed transitions of  $C_2H$  and c- $C_3H_2$ . The quantitative analysis of the data is described in Sect. 4. In Sect. 5, we discuss the results and the main conclusions of this work are summarized in Sect. 6.

#### 2. Observations

### 2.1. The APEX data

Observations of the  $N=3\to 2$  and  $5\to 4$  transitions of  $C_2H$  and  $J_{K_a,K_b}=6_{3,4}\to 5_{2,3}, 7_{1,6}\to 6_{2,5}$  and  $8_{1,8}\to 7_{0,7}$  ortho; and  $7_{2,6}\to 6_{1,5}$  and  $8_{0,8}\to 7_{1,7}$  para transitions of c-C<sub>3</sub>H<sub>2</sub> were performed with the APEX 12 m submillimeter telescope during 2015 June–August and 2016 July and September. As shown in Table 1, we used the following receivers: PI230 with a velocity resolution of 0.07 km s<sup>-1</sup>, to map the  $N=3\to 2$  of  $C_2H$ , which is split into 8 hyperfine structure (hfs) components, FLASH<sup>+</sup> in the 460 GHz band with a velocity resolution of 0.05 km s<sup>-1</sup>, to integrate deeply on the  $N=5\to 4$  of  $C_2H$ , (4 hfs components) toward Her 36 and FLASH<sup>+</sup> in the 345 GHz band with a velocity resolution of 0.04 km s<sup>-1</sup>, to integrate deeply on the  $J_{K_a,K_b}=6_{3,4}\to 5_{2,3}, 7_{1,6}\to 6_{2,5}$  and  $8_{1,8}\to 7_{0,7}$  ortho; and  $7_{2,6}\to 6_{1,5}$  and  $8_{0,8}\to 7_{1,7}$  para transitions of c-C<sub>3</sub>H<sub>2</sub> toward Her 36. To increase the signal-to-noise ratio, the data was later smoothed from a velocity resolution of 0.07 km s<sup>-1</sup> to 0.7 km s<sup>-1</sup>, 0.05 km s<sup>-1</sup> to 0.5 km s<sup>-1</sup> and 0.04 km s<sup>-1</sup> to 0.4 km s<sup>-1</sup>.

The map was observed in on-the-fly (OTF) total power mode centered on R.A. =  $18^h03^m40^s$ .3 and Dec. =  $-24^\circ23'12''(J2000)$  which corresponds to the position of Her 36. It has a size  $\sim 240'' \times 240''$ . Deep integrations were pointed at Her 36 for about  $\sim 3$  minutes while, we integrated 0.7 s per dump for the map. An offset position relative to the center at (30', -30') was chosen for reference, similar to the previous observations done in Tiwari et al. (2018). The pointing accuracy (< 3'') was maintained by pointing checks on bright sources such as Mars and R Dor with the receivers tuned to CO lines every 1–1.5 hrs. A forward efficiency  $\eta_f = 0.95$  was used for all receivers, and the beam coupling efficiencies  $\eta_c = 0.62$ , 0.69 and 0.56 were used for the PI230, FLASH+340 and FLASH+460 receivers, respectively.

### 2.2. The IRAM 30 m data

Observations of the  $N=1\to 0$  transition of  $C_2H$ ; and  $J_{K_a,K_b}=2_{1,2}\to 1_{0,2}$  ortho and  $2_{0,2}\to 1_{1,1}$  transitions of c-C<sub>3</sub>H<sub>2</sub> were performed with the IRAM 30 m telescope in August 2016. Most of the 3 mm range was observed using the EMIR receivers (Carter et al. 2012) with a velocity resolution of 0.65 km s<sup>-1</sup>. Six hfs structure lines of  $C_2H$   $N=1\to 0$  transition were mapped and deep integration pointed observations  $J_{K_a,K_b}=2_{1,2}\to 1_{0,1}$  ortho and  $2_{0,2}\to 1_{1,1}$  para transitions of c-C<sub>3</sub>H<sub>2</sub> were performed toward Her 36.

Similar to APEX observations, the map was observed in OTF total power mode centered on Her 36 and has a size of  $240'' \times 240''$ . Each sub scan lasted 25 s and the integration time on the

<sup>&</sup>lt;sup>1</sup> This publication is based on data acquired with the Atacama Pathfinder EXperiment (APEX). APEX is a collaboration between the Max-Planck-Institut für Radioastronomie, the European Southern Observatory, and the Onsala Space Observatory.

<sup>&</sup>lt;sup>2</sup> Based on observations carried out with the IRAM 30 m telescope. IRAM is supported by INSU/CNRS, the MPG (Germany), and IGN (Spain)

Table 1. Observed hydrocarbons toward M8.

Species	Transition	Frequency (GHz)	$E_{up}/k$ (K)	Instrument	Beam (")	Critical density <sup>a</sup> (cm <sup>-3</sup> )
	$N = 1 \to 0, J = 3/2 \to 1/2, F = 1 \to 1$	87.2841	4.2	IRAM 30m/EMIR	30	$2.5 \times 10^{5}$
	$N = 1 \rightarrow 0, J = 3/2 \rightarrow 1/2, F = 2 \rightarrow 1$	87.3168	4.2	IRAM 30m/EMIR	30	$3.2 \times 10^{5}$
	$N = 1 \to 0, J = 3/2 \to 1/2, F = 1 \to 0$	87.3285	4.2	IRAM 30m/EMIR	30	$9.5 \times 10^{4}$
	$N = 1 \to 0, J = 1/2 \to 1/2, F = 1 \to 1$	87.4019	4.2	IRAM 30m/EMIR	30	$1.1 \times 10^{6}$
	$N = 1 \to 0, J = 1/2 \to 1/2, F = 0 \to 1$	87.4071	4.2	IRAM 30m/EMIR	30	$1.8 \times 10^{5}$
	$N = 1 \to 0, J = 1/2 \to 1/2, F = 1 \to 0$	87.4464	4.2	IRAM 30m/EMIR	30	$2.2 \times 10^{5}$
	$N = 3 \rightarrow 2, J = 7/2 \rightarrow 5/2, F = 3 \rightarrow 3$	261.9781	25.1	APEX/PI230	26	$3.2 \times 10^{4}$
	$N = 3 \rightarrow 2, J = 7/2 \rightarrow 5/2, F = 4 \rightarrow 3$	262.0042	25.1	APEX/PI230	26	$8.7 \times 10^{5}$
$C_2H$	$N = 3 \rightarrow 2, J = 7/2 \rightarrow 5/2, F = 3 \rightarrow 2$	262.0064	25.1	APEX/PI230	26	$8.5 \times 10^{5}$
	$N = 3 \rightarrow 2, J = 5/2 \rightarrow 3/2, F = 3 \rightarrow 2$	262.0649	25.1	APEX/PI230	26	$8.9 \times 10^{5}$
	$N = 3 \rightarrow 2, J = 5/2 \rightarrow 3/2, F = 2 \rightarrow 1$	262.0674	25.1	APEX/PI230	26	$8.2 \times 10^{5}$
	$N = 3 \rightarrow 2, J = 5/2 \rightarrow 3/2, F = 2 \rightarrow 2$	262.0789	25.1	APEX/PI230	26	$1.2 \times 10^{5}$
	$N = 3 \rightarrow 2, J = 5/2 \rightarrow 5/2, F = 3 \rightarrow 3$	262.2086	25.1	APEX/PI230	26	$8.4 \times 10^{4}$
	$N = 3 \rightarrow 2, J = 5/2 \rightarrow 5/2, F = 2 \rightarrow 2$	262.2509	25.1	APEX/PI230	26	$4.9 \times 10^{4}$
	$N = 5 \rightarrow 4, J = 11/2 \rightarrow 9/2, F = 6 \rightarrow 5$	436.661	62.9	APEX/FLASH+ 460	13	$2.9 \times 10^{6}$
	$N = 5 \rightarrow 4, J = 11/2 \rightarrow 9/2, F = 5 \rightarrow 4$	436.6618	62.9	APEX/FLASH+ 460	13	$2.9 \times 10^{6}$
	$N = 5 \rightarrow 4, J = 9/2 \rightarrow 7/2, F = 5 \rightarrow 4$	436.723	62.9	APEX/FLASH+ 460	13	$3.3 \times 10^{6}$
	$N = 5 \rightarrow 4, J = 9/2 \rightarrow 7/2, F = 4 \rightarrow 3$	436.724	62.9	APEX/FLASH+ 460	13	$3.2 \times 10^{6}$
	$J_{K_a,K_b} = 2_{1,2} \rightarrow 1_{0,2}$	85.3388	6.4	IRAM 30m/EMIR	30	$1.1 \times 10^{6}$
c-C <sub>3</sub> H <sub>2</sub> ortho	$J_{K_a,K_b} = 6_{3,4} \rightarrow 5_{2,3}$	285.7956	54.7	APEX/FLASH+ 345	19	$8.4 \times 10^{6}$
2-C3H2 OIUIO	$J_{K_a,K_b} = 7_{1,6} \rightarrow 6_{2,5}$	284.998	61.2	APEX/FLASH+ 345	19	$8.9 \times 10^{6}$
	$J_{\rm K_a, K_b} = 8_{1,8} \to 7_{0,7}$	284.8052	64.3	APEX/FLASH+ 345	19	$1.0 \times 10^{7}$
c-C <sub>3</sub> H <sub>2</sub> para	$J_{K_a,K_b} = 2_{0,2} \rightarrow 1_{1,1}$	82.0935	6.4	IRAM 30m/EMIR	30	$9.9 \times 10^{5}$
	$J_{K_a,K_b} = 7_{2,6} \rightarrow 6_{1,5}$	284.9993	61.2	APEX/FLASH+ 345	19	$1.0 \times 10^{7}$
	$J_{K_a,K_b} = 8_{0,8} \to 7_{1,7}$	284.8052	64.3	APEX/FLASH+ 345	19	$1.0 \times 10^{7}$

<sup>&</sup>lt;sup>a</sup> Critical densities are calculated using collision rates available at  $T_{\rm kin} = 100$  K for C<sub>2</sub>H and at  $T_{\rm kin} = 120$  K for c-C<sub>3</sub>H<sub>2</sub> from Spielfiedel et al. (2012) and Chandra & Kegel (2000) respectively.

off-source reference position was 5 s. The offset position relative to the center at (30', -30') was similar to that used for APEX observations and the pointing accuracy (< 3") was maintained by pointing at the bright calibrator 1757-240 every 1–1.5 hrs. A forward efficiency  $\eta_{\rm f}=0.95$  and the beam coupling efficiency  $\eta_{\rm c}=0.69$  were adopted for EMIR receivers. These values were taken from the (2015) commissioning report<sup>3</sup>.

All data reduction employed the CLASS and GREG softwares that are a part of the GILDAS<sup>4</sup> software package and all observations are summarized in Table 1.

**Table 2.** Hfs fit parameters of the observed low and high velocity components of  $C_2H$ .

Transition	on $v^{a}(\text{km s}^{-1})$ $\Delta v^{a}(\text{km s}^{-1})$ $T_{\text{mb}}^{a}($		$T_{\rm mb}^{\rm a}({\rm K})$	$ au^{\mathrm{a}}$				
Low velocity component								
$N = 5 \rightarrow 4$	5.9 (0.524)	1.63 (1.74)	0.9 (0.053)	0.78 (0.1)				
High velocity component								
$N = 1 \rightarrow 0$	9.5 (0.0025)	3.43 (0.014)	2.5 (0.018)	$\sim 0.1^{b}$				
$N=3\rightarrow 2$	8.8 (0.013)	4.52 (0.046)	4.5 (0.031)	1.74 (0.102)				
$N = 5 \rightarrow 4$	9.6 (0.524)	3.45 (1.74)	2.6 (0.053)	~ 0.1 <sup>b</sup>				

<sup>&</sup>lt;sup>a</sup> The values in the parenthesis indicate the errors from the fit.

#### 3. Results

### 3.1. Ethynyl: C<sub>2</sub>H

The ethynyl radical  $(C_2H)$  was first detected in the ISM by Tucker et al. (1974). It is a linear molecule with spin rotation

and hyperfine structure. The energy levels are designated as N, Jand F. The coupling between the rotational angular momentum N and the unpaired electron spin S, causes spin doubling (J = N)+ S), while the coupling of angular momentum J and spin of the hydrogen nucleus I, results in hfs (F = J + I) (Cuadrado et al. 2015). The electric dipole selection rules allow hfs splitting to occur only in specific quantum levels. We were able to identify a total of 18 hfs components of C<sub>2</sub>H and the line parameters derived from hfs fitting. The C<sub>2</sub>H  $N = 1 \rightarrow 0$  and  $3 \rightarrow 2$  transitions have a single velocity component, while  $C_2H N = 5 \rightarrow 4$  also have a spectrally resolved low velocity (2–8 km s<sup>-1</sup>) component, in addition to a high velocity (8–15 km s<sup>-1</sup>) component. This low velocity component is also seen in the CO, [C II] and [C I] spectra and corresponds to the warm foreground veil receding away from Her 36 toward the observer (Tiwari et al. 2018). The hfs fit parameters of the observed low and high velocity components of C<sub>2</sub>H are given in Table 2.

The hfs line fitting results for all the transitions are shown in Fig. 1. The lowest energy rotational transition  $N=1\to 0$  is split into 6 observable hfs levels that are well separated in frequency. The observed relative intensities are listed in Table A.1 and it can be seen except for the lowest intensity lines, all match well with the expected relative intrinsic intensities as obtained from the Cologne Database for Molecular Spectroscopy<sup>5</sup> (CDMS). Hence, the lines are optically thin with no hfs emission anomalies and consistent with an optical depth of  $\tau \sim 0.1$ . For the  $N=3\to 2$  rotational transition, we identified 8 hfs components. Among them, some hfs features are not completely resolved and hence, some lines overlap. The  $J=7/2\to 5/2$ ,  $F=4\to 3$  and  $F=3\to 2$  overlap; and the  $J=5/2\to 3/2$ ,  $F=3\to 2$  and  $F=2\to 1$  overlap. The observed relative line intensities come out to be different from the expected relative intensities

 $<sup>^{\</sup>rm b}$  0.1 is the lower limit value of au calculated by GILDAS for optically thin emission.

<sup>&</sup>lt;sup>3</sup> www.iram.es/IRAMES/mainWIKI/IRAM30mEfficiencies

<sup>4</sup> www.iram.fr/IRAMFR/GILDAS/

<sup>&</sup>lt;sup>5</sup> http://www.astro.uni-koeln.de/cdms/

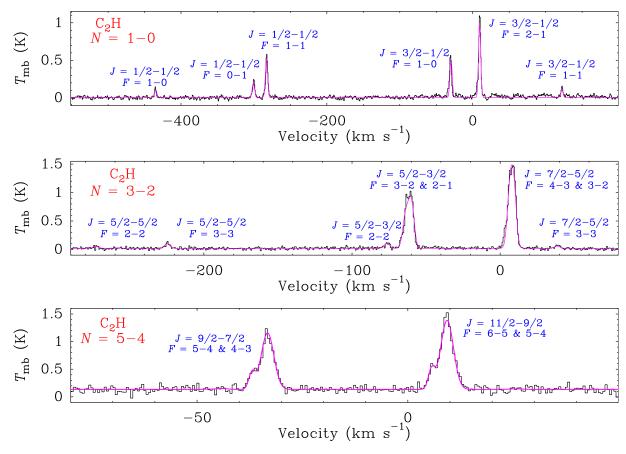


**Fig. 1.** Observed hfs components of the  $N=1\to 0$ ,  $3\to 2$ ,  $5\to 4$  rotational transitions of  $C_2H$  toward Her 36 at R.A.  $18^h03^m40^s.3$ ; Dec.  $-24^\circ22'43''$  (J2000). For the  $N=1\to 0$  transition all 6 hfs are fully resolved, while for the  $N=3\to 2$  and  $5\to 4$  transitions, some hfs lines overlap with each other. The  $N=5\to 4$  shows an additional spectrally resolved velocity component (2–8 km s<sup>-1</sup>) compared to other transitions. Only the detected lines are indicated by their quantum numbers J and F.

except for the higher transitions as shown in Table A.1. This suggests optical depth effects and indeed an optical depth of  $\tau \sim 1.74$  was calculated. For the  $N=5 \to 4$  rotational transition, we identified 4 hfs components where the lines with  $J=9/2 \to 7/2$ ,  $F=5 \to 4$  and  $F=4 \to 3$ ; and the lines  $J=11/2 \to 9/2$ ,  $F=6 \to 5$  and  $F=5 \to 4$  overlap. The observed relative intensities match well with the expected relative intrinsic intensities and are consistent within optical depth  $\tau \sim 0.1$ .

#### 3.2. Cyclopropenylidene: c- $C_3H_2$

Cyclopropenylidene, c- $C_3H_2$ , was first discovered in the ISM by Matthews & Irvine (1985) and Thaddeus et al. (1985). It is a three-membered carbon ring with  $C_{2v}$  symmetry (see Spezzano et al. 2012, Fig. 1), with a large dipole moment of 3.4 Debye making it highly polar. It has ortho and para symmetries owing to the two out of plane hydrogen atoms, which are at equidistant from the C atoms. It is an oblate asymmetric top with b-type rotational transitions where the main selection rules are  $\Delta K_a$  and  $\Delta K_c = \pm 1$ .  $K_a + K_c = \text{odd/even}$  values correspond to the ortho/para levels (for more extensive description see Cuadrado et al. 2015).

We observed 2 completely resolved ortho transitions  $J_{K_a,K_b} = 2_{1,2} \rightarrow 1_{0,1}$  and  $6_{3,4} \rightarrow 5_{2,3}$  and 1 para transition  $J_{K_a,K_b} = 2_{0,2} \rightarrow 1_{1,1}$ . In addition, we observed  $J_{K_a,K_b} = 7_{1,6} \rightarrow 6_{2,5}$  and  $8_{1,8} \rightarrow 7_{0,7}$  ortho; and  $7_{2,6} \rightarrow 6_{1,5}$  and  $8_{0,8} \rightarrow 7_{1,7}$  para transitions where ortho and para lines are blended. Similar to the  $N = 5 \rightarrow 4$  transition of  $C_2H$ , all observed transitions of  $c-C_3H_2$  have a spectrally

**Table 3.** C<sub>3</sub>H<sub>2</sub> line parameters as calculated from two component gaussian fit using GILDAS.

_	0 1.	1.	_ 0/ ==:					
<u> </u>		. ,	$T_{\text{peak}}^{\text{a}}(\mathbf{mK})$					
Low velocity component								
ortho	6.0 (0.22)	2.3 (0.43)	90 (18)					
para	7.2 (0.62)	2.0(0)	40 (17)					
ortho	6.3 (1.0)	2.7 (1.3)	20 (23)					
ortho	5.5 (0.3)	3.1 (0.7)	50 (13)					
para	5.5 (0.3)	3.1 (0.7)	50 (13)					
ortho	6.0(0.2)	1.9 (0.5)	80 (20)					
para	para 6.0 (0.2) 1.9 (0.5)		80 (20)					
High velocity component								
ortho	10 (0.07)	3.17 (0.2)	300 (18)					
para	10.5 (0.2)	2.6 (0.4)	100 (17)					
ortho	10.1 (0.3)	3.3 (1.2)	50 (23)					
ortho	10.2 (0.15)	2.7 (0.4)	100 (13)					
para	10.2 (0.15)	2.7 (0.4)	100 (13)					
ortho	10.3 (0.15)	3.6 (0.4)	130 (20)					
$8_{0,8} \to 7_{1,7}$ para		3.6 (0.4)	130 (20)					
	ortho para ortho ortho para ortho para  Hig  ortho para  ortho para ortho para ortho ortho para ortho	Tow velocity comports of the c	Low velocity component					

<sup>&</sup>lt;sup>a</sup> The values in the parenthesis indicate the errors from the fit.

resolved low velocity component (centered at  $\sim 6~{\rm km~s^{-1}}$ ) as can be seen in Fig. 2. The line parameters are derived from a two component gaussian fit to the observed spectra as mentioned in Table 3.

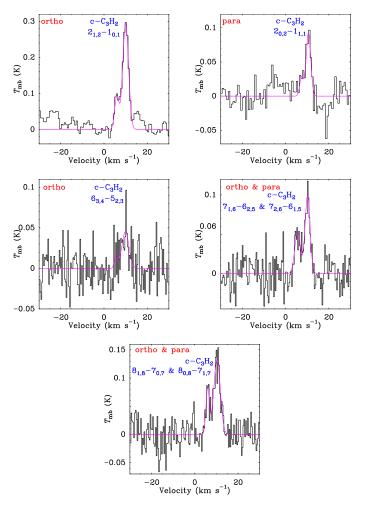


**Fig. 2.** Observations of spectrally resolved  $J_{\rm K_a,K_b}=2_{1,2}\to 1_{0,1}$  and  $6_{3,4}\to 5_{2,3}$  ortho and  $J_{\rm K_a,K_b}=2_{0,2}\to 1_{1,1}$  para transitions of c-C<sub>3</sub>H<sub>2</sub> along with the spectrally blended  $7_{1,6}\to 6_{2,5}$  and  $8_{1,8}\to 7_{0,7}$  ortho; and  $7_{2,6}\to 6_{1,5}$  and  $8_{0,8}\to 7_{1,7}$  para transitions toward Her 36 at R.A.  $18^h03^m40^s.3$ ; Dec.  $-24^\circ22'43''$  (J2000).

# 3.3. Spatial distribution of $C_2H$ and comparison with ancillary data

Figure 3 shows velocity integrated intensity maps of the brightest transitions of C<sub>2</sub>H  $N=1\rightarrow 0, J=3/2\rightarrow 1/2, F=2\rightarrow 1$ at 87.316 GHz with an rms noise of 0.3 K km s<sup>-1</sup> and N = 3 $\rightarrow$  2  $J = 7/2 \rightarrow 5/2$ ,  $F = 4 \rightarrow 3$  at 262.004 GHz with an rms noise of 0.44 K km s<sup>-1</sup>. The  $N = 1 \rightarrow 0$  transition is bright toward the north-west of Her 36 and peaks (in projection) deep into the molecular cloud at  $(\Delta \alpha = -56'', \Delta \delta = 28'')$ . This position is very close to the secondary ATLASGAL 870 μm dust continuum peak toward this region at  $(\Delta \alpha = -53'', \Delta \delta = 23'')$  (Tiwari et al. 2018, Fig. 7 (a)) which is probing the cold molecular cloud. The  $N=3\rightarrow 2$  transition is brightest close to Her 36 at  $(\Delta\alpha=0'',\Delta\delta)$ = 12") with the emission extending toward north-west of Her 36. The hot gas near Her 36 would be able to excite C<sub>2</sub>H molecule to rotational levels with higher upper level energies whereas the gas deep into the molecular cloud would be comparatively cooler. It is noteworthy that the extended emission, as shown in Fig. B.1, toward the north-west of Her 36 is also seen in low and mid-J CO transitions and in [C<sub>I</sub>] observed toward M8 by the APEX and IRAM 30 m telescopes (Tiwari et al. 2018).

In order to investigate the relation of the dense and cold molecular cloud material to the hot ionized gas in M8, we com-

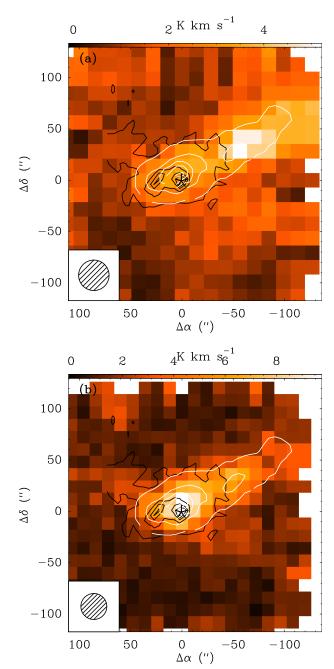


Fig. 3. Colour maps of the velocity integrated intensity of the: (a, upper panel)  $N=1 \rightarrow 0$  and (b, lower panel)  $3 \rightarrow 2$  transitions of  $C_2H$  toward Her 36 which is the central position ( $\Delta \alpha=0$ ,  $\Delta \delta=0$ ) at R.A.(J2000) =  $18^h03^m40.3^s$  and Dec.(J2000) =  $-24^\circ22'43''$ , marked with an asterisk. Both maps are plotted using original beam sizes shown in the bottom left of each map. These maps are overlaid with contours of GLIMPSE 8  $\mu m$  continuum emission in black, with a beam size of 0.6" and with contours of SPIRE 250  $\mu m$  continuum emission in white, with a beam size of 17.9". For GLIMPSE 8  $\mu m$  continuum emission, the contour levels are 10% to 100% in steps of 20% of the peak emission and for SPIRE 250  $\mu m$  continuum emission, the contour levels are 10% to 100% in steps of 10% of the peak emission.

pared our observed  $C_2H$  data with observations obtained from 2 surveys conducted at different wavelengths. Firstly, we used the 8  $\mu$ m data from the Galactic Legacy Infrared Mid-Plane Survey Extraordinaire (GLIMPSE, Benjamin et al. 2003) archive observed with Spitzer Space Telescope. The 8  $\mu$ m band of the Infrared Array Camera (IRAC) used by Spitzer covers emission

from polycyclic aromatic hydrocarbons (PAHs) which are small molecules excited by strong UV radiation. Since the IR emission from these large molecules (or small dust grains) constitutes fluorescence that results from far-UV pumping, it emerges from the surface layers of dense molecular clouds, PAH emission probes recent high-mass star formation (Tielens 2008). Figure 3 shows the velocity integrated intensity maps of  $C_2H \rightarrow 0$  and  $3 \rightarrow 2$ transitions in color scale overlaid with GLIMPSE 8  $\mu$ m contours in black, which peaks at Her 36 ( $\Delta \alpha = 0''$ ,  $\Delta \delta = 0''$ ) and at the [C II] emission peak ( $\Delta \alpha = 30''$ ,  $\Delta \delta = -2''$ ). [C II] was observed in May 2016 by the SOFIA telescope and the data has been reported in (Tiwari et al. 2018). Secondly, we obtained, from the Herschel Space Archive<sup>6</sup> (HSA), data collected with the Spectral and Photometric Imaging Receiver (SPIRE, Griffin et al. 2010) aboard the Herschel Space Observatory (Pilbratt et al. 2010). The SPIRE data trace interstellar dust. The white contours in Fig. 3 represent the SPIRE 250  $\mu$ m continuum emission, which peaks at Her 36 ( $\Delta \alpha = 0^{\prime\prime}$ ,  $\Delta \delta = 0^{\prime\prime}$ ) and is extended in northwest direction with a secondary peak coinciding the peak of the  $C_2H \rightarrow 0$  emission ( $\Delta \alpha = -56''$ ,  $\Delta \delta = 28''$ ).

#### 4. Analysis

Various transitions of  $C_2H$  and  $c\text{-}C_3H_2$  observed with the IRAM 30 m and APEX 12 m telescopes allow us to carry out a detailed analysis to determine the temperature and density of the gas responsible for the emission of hydrocarbons in M8 with several complementary methods. We started with estimating the excitation temperature and the total  $C_2H$  column density by using its OTF maps of  $1 \to 0$  and  $3 \to 2$  transitions in Sect. 4.1. We then calculated column densities and abundances of both  $C_2H$  and  $c\text{-}C_3H_2$  from rotational diagrams in Sect. 4.2. To complete the analysis, we made use of a radiative transfer model to constrain the  $H_2$  densities in M8 in Sect. 4.3 and compared our observed results with PDR models in Sect. 4.4.

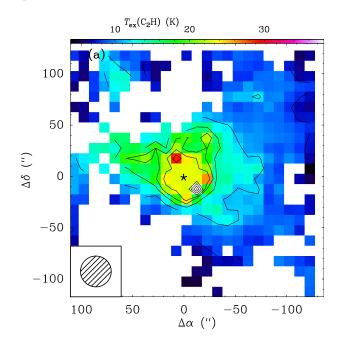
## 4.1. Excitation temperature and column density estimates of

Assuming a beam filling factor of unity and optically thin emission in both the C<sub>2</sub>H  $N=1 \rightarrow 0$ ,  $J=3/2 \rightarrow 1/2$ ,  $F=2 \rightarrow 1$  at 87.316 GHz and  $N=3 \rightarrow 2$   $J=7/2 \rightarrow 5/2$ ,  $F=4 \rightarrow 3$  at 262.004 GHz transitions, the excitation temperature can be estimated by:

$$T_{\rm ex} = \frac{-20.95}{\ln(0.144 \frac{W_3}{W_*})} K, \qquad (1)$$

where  $W_1$  and  $W_3$  are the velocity integrated intensities in K cm s<sup>-1</sup> of  $N=1 \rightarrow 0$  and  $3 \rightarrow 2$  transitions of C<sub>2</sub>H respectively. The resulting  $T_{\rm ex}$  distribution is shown in Fig. 4 (a), and these are only lower limits to the excitation temperature as the beam filling factor is assumed to be unity. The peak of the  $T_{\rm ex}$  distribution  $\sim 38~{\rm K} \pm 11~{\rm K}$  lies in the immediate south-west of Her 36 ( $\Delta \alpha = -15''$ ,  $\Delta \delta = -13''$ delta) and  $T_{\rm ex}$  decreases with the distance from the star.

Assuming the environment to be in Local Thermodynamical Equilibrium (LTE) such that all transitions have the same excitation temperature and that  $T_{\rm ex}$  equals the molecule's rotation temperature,  $T_{\rm rot}$ , we calculated the total column density of C<sub>2</sub>H



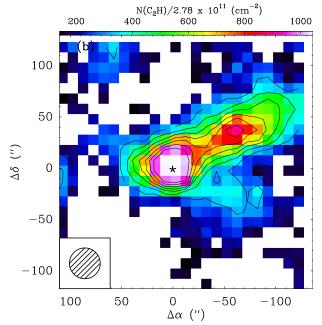


**Fig. 4.** (a, upper panel) shows the excitation temperature defining the populations of N=1 and 3 levels and (b, lower panel) shows the total column density of  $C_2H$ . The asterisk represents Her 36 which is the central position ( $\Delta\alpha=0$ ,  $\Delta\delta=0$ ) at R.A.(J2000) =  $18^h03^m40.3^s$  and Dec.(J2000) =  $-24^\circ22'43''$ . The contour levels are 10% to 100% in steps of 10% of the corresponding peak emissions. The values of main beam brightness temperatures and that of the velocity integrated intensities for the N=1 and 3 levels used to calculate the  $T_{\rm ex}(C_2H)$  and  $N(C_2H)$  were extracted from maps convolved to the same resolution of 30".

using the computed  $T_{\rm ex}$  and the velocity integrated intensity,  $W_3$ , of  $N=3\to 2$  transition of  $C_2H$ :

$$N(C_2H) = 2.78 \times 10^{11} (1.9 T_{\text{ex}} + 1.38) \exp\left(\frac{25.15}{T_{\text{ex}}}\right) W_3 \text{ cm}^{-2}$$
. (2)

Figure 4 (b) shows the resulting  $C_2H$  total column density distribution with a peak value of  $N(C_2H) \sim (3 \pm 0.26) \times 10^{14}$ 

<sup>&</sup>lt;sup>6</sup> https://irsa.ipac.caltech.edu/applications/Herschel/

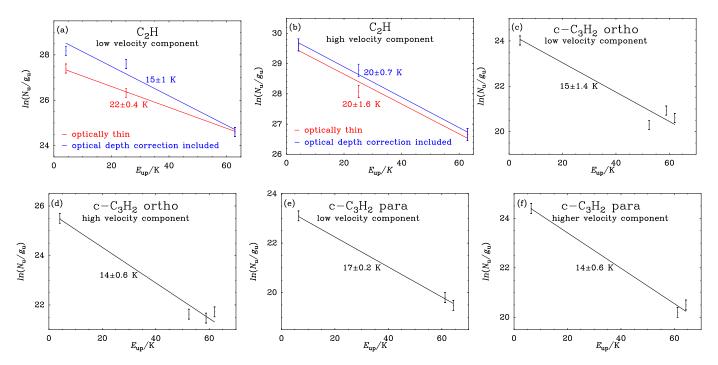


Fig. 5. Rotational diagrams of various transitions of the  $N = 1 \rightarrow 0$ ,  $3 \rightarrow 2$  and  $5 \rightarrow 4$  transitions of  $C_2H$  (top row);  $J = 2 \rightarrow 1$ ,  $6 \rightarrow 5$ ,  $7 \rightarrow 6$  and  $8 \rightarrow 7$  transitions of ortho c- $C_3H_2$  (top and bottom rows); and  $J = 2 \rightarrow 1$ ,  $7 \rightarrow 6$  and  $8 \rightarrow 7$  transitions of para c- $C_3H_2$  (bottom row) observed toward Her 36. For  $C_2H$ , rotational diagrams are plotted with an assumption of optically thin  $C_2H$  (in red) and with including the optical depth correction factors (in blue). Fitted values of rotational temperatures are given for each molecule. The error bars were calculated from the maximum noise of the integrated intensities of individual transitions and from calibration uncertainties of 20%.

**Table 4.** Physical parameters calculated from rotational diagrams.

Species	Lower velocity component		Higher	velocity component	Abundance
	$T_{\rm rot}$ (K)	$N(X) \text{ (cm}^{-2})$	$T_{\rm rot}$ (K)	$N(X) \text{ (cm}^{-2})$	$N(X)/N(H_2)$
C <sub>2</sub> H(optically thin)	$22 \pm 0.4$	$(3.8 \pm 0.2) \times 10^{13}$	$20 \pm 1.6$	$(2.9 \pm 0.1) \times 10^{14}$	$(0.9 \pm 0.04) \times 10^{-8}$
C <sub>2</sub> H(optical depth correction included)	$15 \pm 1$	$(9.8 \pm 0.5) \times 10^{13}$	$20 \pm 0.7$	$(3.8 \pm 0.3) \times 10^{14}$	$(1.3 \pm 0.1) \times 10^{-8}$
$c-C_3H_2$ - ortho	$15 \pm 1.4$	$(4 \pm 0.1) \times 10^{12}$	$14 \pm 0.6$	$(1.8 \pm 0.43) \times 10^{13}$	$(6 \pm 1.2) \times 10^{-10}$
c-C <sub>3</sub> H <sub>2</sub> - para	$17 \pm 0.2$	$(2.2 \pm 0.1) \times 10^{12}$	$14 \pm 0.6$	$(7.2 \pm 0.2) \times 10^{12}$	$(2.5 \pm 0.1) \times 10^{-10}$

cm<sup>-2</sup> at Her 36 and a secondary peak toward the north-west of Her 36 in the molecular cloud similar to the secondary ATLAS-GAL peak. This results in an abundance of  $N(C_2H)/N(H_2) \sim 8 \times 10^{-8}$ , where we adopted  $N(H_2) \sim 3.75 \times 10^{22}$  cm<sup>-2</sup> (Tiwari et al. 2018).

#### 4.2. Rotational Diagrams of C<sub>2</sub>H and c-C<sub>3</sub>H<sub>2</sub>

In Sect. 4.1, we presented the maps of excitation temperature and total column density distribution of  $C_2H$  in M8, around Her 36. But c- $C_3H_2$  and the higher transition of  $C_2H$  were a part of point observations done by integrating deeply toward Her 36. So, we exploit the technique of rotational diagrams to perform a detailed analysis of more transitions as compared to Sect. 4.1. Also, here we plot rotational diagrams for both low and high velocity components of all observed transitions of  $C_2H$  and c- $C_3H_2$  observed toward Her 36. Assuming LTE, rotational diagrams ("Boltzmann plots") can be used to estimate the total column densities,  $N_{\text{tot}}$ , of  $C_2H$  and c- $C_3H_2$  and the rotation temperatures,  $T_{\text{rot}}$  describing their level populations (Goldsmith & Langer 1999). In a rotational diagram,  $ln(N_u/g_u)$  is plotted vs.  $E_{up}/k$ . Here,  $ln(N_u)$  and  $g_u (\equiv 2J + 1)$  are the column density in and the degeneracy of

the upper energy level, respectively,  $E_{\rm up}$  is the upper level energy and k is the Boltzmann constant.

Given the extended emission seen in the velocity integrated intensity maps in Fig. 3, we adopted a beam filling factor of 1 to make rotational diagrams. Moreover, we assume the hfs lines of each rotational transition to be treated as a single component with a quantum number N. We then calculated the total velocity integrated intensity, the upper level degeneracy  $g_{\rm u}$  and the line strength of different transitions as the sum of all the observed hfs components of each  $N+1 \rightarrow N$  transition. Using the weighted average with the relative strength of each line as weight, the hfsweighted frequency  $\nu$  was obtained (as in Cuadrado et al. 2015) and the Einstein coefficient A was calculated using Goldsmith & Langer (1999, Eq. 25).

**Figures 5 (a) and (b)** show rotational diagrams of  $C_2H$  for low (2–8 km s<sup>-1</sup>) and high (8–15 km s<sup>-1</sup>) velocity components respectively. Firstly, under the assumption that the  $C_2H$  lines are optically thin, i.e. the optical depth correction term  $C_\tau$  is unity in Goldsmith & Langer (1999, Eq. 24), we plotted  $N_u^{\text{thin}}/g_u$  vs.  $E_{up}/k$  in red for three transitions toward Her 36. Since the low velocity component could only be spectrally resolved for the  $N = 5 \rightarrow 4$  transition, we estimated the low velocity component's line parameters for the other transitions assuming the same ve-

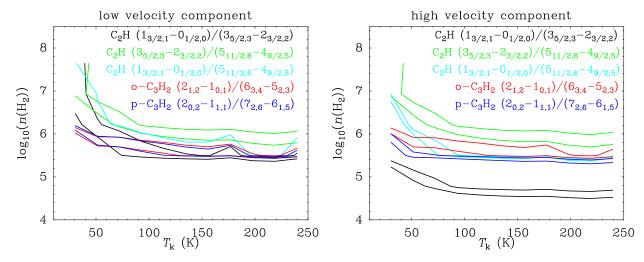


Fig. 6. Results obtained from RADEX modeling for the main beam brightness temperature ratios of various transitions of  $C_2H$  and c- $C_3H_2$  toward Her 36 in a  $\log_{10}(n(H_2))$  vs  $T_k$  grid. The left and right panels correspond to the low velocity and the high velocity components respectively. The two contours per color represent the RADEX modeling output values equal to the upper and lower bounds of the value obtained for each ratio from the observations with an error of 20%.

locity and line width as that of  $N=5\to 4$ . Subsequently, we plotted the corrected diagrams, in blue, by including the optical depth correction values according to Goldsmith & Langer (1999, Eq. 24). The optical depth values were obtained from the hfs fit and are listed in Table 2.

Figures 5 (c), (d), (e) and (f) show rotational diagrams of the ortho and para species of c-C<sub>3</sub>H<sub>2</sub> for the low (2–8 km s<sup>-1</sup>) and high (8–15 km s<sup>-1</sup>) velocity components. We first assumed  $\text{c-C}_3\text{H}_2$  to be optically thin and from  $J_{\text{K}_a,\text{K}_b} = 2_{1,2} \rightarrow 1_{0,1}$  ortho and  $J_{K_a,K_b} = 2_{0,2} \rightarrow 1_{1,1}$  para transitions, we calculated the ortho/para ratio ~ 2.2 for low velocity component and 3.3 for high velocity component. These ratios were used to estimate the contributions from ortho and para species to the  $J_{K_a,K_b} = 7_{1,6} \rightarrow 6_{2,5}$ and  $8_{1,8} \rightarrow 7_{0,7}$  ortho; and  $7_{2,6} \rightarrow 6_{1,5}$  and  $8_{0,8} \rightarrow 7_{1,7}$  para transitions, where the lines from the two species are blended together as can be seen in Fig. 2. From the obtained rotational temperatures, we estimated the column densities of C<sub>2</sub>H and c-C<sub>3</sub>H<sub>2</sub>, which in turn were used to determine the optical depths of c-C<sub>3</sub>H<sub>2</sub> (Goldsmith & Langer 1999, Eq. 27). The estimated optical depth values came out to be very low, validating our assumption of optically thin  $c-C_3H_2$ .

The calculated rotational temperatures  $T_{\rm rot}$  and column densities  $N({\rm X})$  along with their abundances  $N({\rm X})/N({\rm H_2})$  of  ${\rm C_2H}$  and c-C<sub>3</sub>H<sub>2</sub> are given in Table 4. The total column density value of C<sub>2</sub>H at the Her 36 position calculated using the rotational diagrams is very similar to that determined in Sect. 4.1.

#### 4.3. Non-LTE calculations

In Sects. 4.1 and 4.2, we obtained the column densities and abundances of  $C_2H$ , o- $C_3H_2$  and p- $C_3H_2$  under the assumption of LTE. The derived rotational temperatures ( $\sim 15$ –20 K) are much lower than values that one might expect in the vicinity of Her 36 and temperatures derived in our previous study (Tiwari et al. 2018). This could be caused by the fact that the critical densities of the higher  $E_{\rm up}$  lines of  $C_2H$  and  $C_3H_2$  are much higher than those of the lower  $E_{\rm up}$  lines of both molecules. This leads to subthermal excitation of the higher  $E_{\rm up}$  lines and, consequently, to lower than LTE integrated intensities (and lower  $N_{\rm up}/g_{\rm up}$  values). This results in a steepening of the fitted line whose slope gives  $T_{\rm rot}$  and an underestimation of that quantity. Therefore the

resultant rotation temperature and column densities should only be considered as guiding values. To address this issue, we employ a non-LTE analysis that delivers kinetic temperature and H<sub>2</sub> volume densities of the gas that gives rise to the emission of C<sub>2</sub>H and C<sub>3</sub>H<sub>2</sub>. RADEX is a non-LTE radiative transfer program (van der Tak et al. 2007), which uses the escape probability approximation for a homogeneous medium and takes into account optical depth effects. We chose a uniform sphere geometry. The collision rates used in the modeling are provided by the Leiden Molecular and Atomic Database<sup>7</sup> (LAMDA; Schöier et al. (2005)). The C<sub>2</sub>H-H<sub>2</sub> collision rates are calculated by multiplying a factor of 1.36 to the C<sub>2</sub>H-He collision rates given by Spielfiedel et al. (2012), while the C<sub>3</sub>H<sub>2</sub>-H<sub>2</sub> collision rates are given by Chandra & Kegel (2000). We computed grids in kinetic temperatures in the range 20–250 K and H<sub>2</sub> volume densities in the range  $10^3 - 10^8$  cm<sup>-3</sup> and a background temperature of 2.73 K as input parameters and then calculated brightness temperature ratios of different transitions of C<sub>2</sub>H, o-C<sub>3</sub>H<sub>2</sub> and p-C<sub>3</sub>H<sub>2</sub>.

We adopted the line widths from the average spectra of our data of  $C_2H$ , o- $C_3H_2$  and p- $C_3H_2$  i.e. 3, 2.5, 2.2 km s<sup>-1</sup> respectively for the low velocity  $(2-8 \text{ km s}^{-1})$  component and 3.6, 3.3, 3 km s<sup>-1</sup> respectively for the high velocity (8–15 km s<sup>-1</sup>) component. For modeling, we used the C<sub>2</sub>H, o-C<sub>3</sub>H<sub>2</sub> and p-C<sub>3</sub>H<sub>2</sub> column densities as estimated from the rotational diagrams in Sect. 4.2 i.e.  $7 \times 10^{13}$ ,  $7 \times 10^{12}$  and  $4 \times 10^{12}$  cm<sup>-2</sup> respectively for the low velocity component and  $4 \times 10^{14}$ ,  $2 \times 10^{13}$  and  $7 \times$ 10<sup>12</sup> cm<sup>-2</sup> respectively for the high velocity component. Figure 6 shows the brightness temperature ratios (in different colors) of various transitions of  $C_2H$ , o- $C_3H_2$  and p- $C_3H_2$  on a  $log_{10}(n(H_2))$ vs.  $T_{\rm kin}$  plot. The two different contours per color represent the RADEX modeling output values equal to the upper and lower bounds of the value obtained for each ratio from the observations with an error of 20%. For low  $T_{\rm kin}$  (20–100 K), a gradient in density is seen, which then almost saturates for higher  $T_{kin}$ (100-250 K).

For very low temperatures  $T_{\rm kin}$  < 50 K, the H<sub>2</sub> volume density  $n({\rm H_2})$  is as high up to  $5 \times 10^7$  cm<sup>-3</sup>. But in our previous work, we determined kinetic temperatures  $T_{\rm kin} \sim 100$ –150 K in M8 (Tiwari et al. 2018, Sect. 4.3), which puts a constraint on the

<sup>&</sup>lt;sup>7</sup> http://www.strw.leidenuniv.nl/moldata/

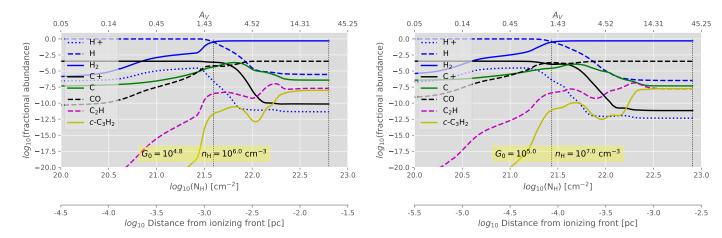


**Fig. 7.** PDR models for M8 for  $G_0 = 10^{4.8}$  and  $n_{\rm H} = 10^5$  cm<sup>-3</sup> (left panel) and  $G_0 = 10^5$  and  $n_{\rm H} = 10^7$  cm<sup>-3</sup> (right panel). The fractional abundances  $(n_X/n_{\rm H})$  are represented by the color codes/lines patterns indicated on the plots and measured by the ordinates. The top abscissa indicates the corresponding visual extinction  $(A_{\rm V})$  as seen from the ionizing front (the impinging radiation field goes from left to right of the plot). The first bottom abscissa gives the corresponding total hydrogen column density  $N({\rm H})$ . A second bottom abscissa shows the actual distance (in pc) from the ionizing front. The vertical dashed lines demarcate the region where most of the hydrogen gas is in molecular form.

volume density  $n(H_2)$  values. For the low velocity component shown in Fig. 6 (a), all hydrocarbons probe similar gas that is a part of the foreground veil, which has been found by and discussed in Tiwari et al. (Sect. 5.1 2018, Fig. 15). The foreground veil accelerating toward us by the strong radiation and wind of Her 36, which is a part of the cold dense molecular cloud has  $H_2$  volume density  $n(H_2)$  in a range of  $5 \times 10^5 - 5 \times 10^6$  cm<sup>-3</sup>. For the high velocity component shown in Fig. 6 (b), the different ratios of C<sub>2</sub>H probe gas of different densities. For  $T_{\rm kin}$  ~ 100–150 K,  $C_2H$  (1  $\rightarrow$  0)/(5  $\rightarrow$  4) probe the same gas as o- $C_3H_2$ and p-C<sub>3</sub>H<sub>2</sub> with  $n(H_2) \sim 1 \times 10^6 \text{ cm}^{-3}$ , while C<sub>2</sub>H (3  $\rightarrow$  2)/(5  $\rightarrow$  4) probe slightly denser gas with  $n(H_2) \sim 5 \times 10^6$  cm<sup>-1</sup> and  $C_2H$  (1  $\rightarrow$  0)/(3  $\rightarrow$  2) probe lower density gas with  $n(H_2) \sim 5 \times$ 10<sup>4</sup> cm<sup>-3</sup>. This velocity component with an H<sub>2</sub> volume density  $n(\rm{H}_2)$  in the range of  $5 \times 10^4 - 5 \times 10^6$  cm<sup>-3</sup>, consists of the gas very close to Her 36 and also the background material toward north-east of it (Tiwari et al. 2018, Sect. 5.1).

#### 4.4. Comparison with PDR models

In order to compare the results obtained with the LTE and non-LTE models, we use PDR models to estimate the relative abundances of the C<sub>2</sub>H and C<sub>3</sub>H<sub>2</sub> species. These PDR models are based on Meijerink & Spaans (2005) which include more than 300 species in the chemical network, photo-electric heating from PAHs and small dust grains, cosmic-ray heating, and other classical heating and cooling mechanism for the thermal and chemical balance. A semi infinite slab geometry and irradiation from one side without geometrical dilution are assumed. Note that the PDR models do not distinguish between ortho and para molecules, but they provide the total abundance of  $C_3H_2$  (and all other available species) self-consistently depending on the depth and visual extinction of the parallel slab. The model uses total gas density  $n_{\rm H} = n({\rm H}) + 2n({\rm H}_2)$ , as an input parameter and the actual density of the collisional partner, molecular hydrogen,  $n(H_2)$  is calculated self-consistently along with the densities of other species from chemical and thermal balance equations, and is depth dependent.

We model four scenarios with two different total gas densities,  $n_{\rm H}$ , and two levels of strength of the impinging radiation field,  $G_0$ , in Habing units. In the models we assume solar metal-

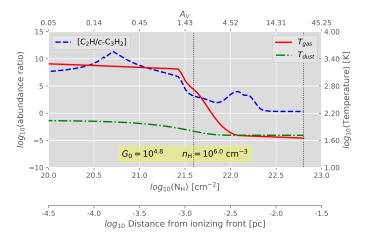
licity and the visual extinction is estimated using the up-to-date relation  $N(H) = 2.21 \times 10^{21} \text{ cm}^{-2} \times A_V$  found by Güver & Özel (2009).

For  $G_0$ , we used the values  $0.6 \times 10^5$  and  $1.12 \times 10^5$  estimated in our previous paper (Tiwari et al. 2018, Sect. 5.2), using Tielens (2008, Eq. 9.2) for an O star with electron density,  $n_{\rm e}$ , of 2000–4000 cm<sup>-3</sup> and electron temperature,  $T_{\rm e}$ , of 7000–9000 K (Woodward et al. 1986; Esteban et al. 1999). We need to use quite high total gas densities  $n_{\rm H}$  of  $10^6$  and  $10^7$  cm<sup>-3</sup> in order to reach densities of the collision partner  $n({\rm H_2})$  similar to the values found in Sect. 4.3 using RADEX. Figure 7 shows the models with the lowest density and impinging radiation field (*left*) and with the highest density and radiation field (*right*) tested.

For the highest density model ( $n_{\rm H}=10^7~{\rm cm}^{-3}$ ) we get relative abundances between  $4\times 10^{-9}$  and  $2\times 10^{-8}$  for  ${\rm C_2H}$  and between  $8\times 10^{-8}$  and  $2\times 10^{-8}$  for  ${\rm C_3H_2}$ , in the region where  ${\rm H_2}$  is more abundant than H (i.e., where  ${\rm H_2}$  becomes the main collision partner, indicated with vertical dashed lines in Fig. 7). Integrating from the layer where  $n({\rm H_2}) \ge n({\rm H})$  to the far edge of the slab, we get column densities of about  $2\times 10^{15}~{\rm cm}^{-2}$  for  ${\rm C_2H}$  and  $10^{15}~{\rm cm}^{-2}$  for  ${\rm C_3H_2}$ . That is, about three times and twenty five times larger than what we found from the rotational diagrams.

For the lowest density model ( $n_{\rm H}=10^6~{\rm cm}^{-3}$ ) we get relative abundances between  $3\times10^{-9}$  and  $2\times10^{-8}$  for C<sub>2</sub>H and between  $2\times10^{-12}$  and  $10^{-8}$  for C<sub>3</sub>H<sub>2</sub>, in the region where  $n({\rm H_2})$  is dominant (i.e., for  $A_{\rm V}$  between 1.8 and 28.6 mag, indicated by the vertical dashed lines in Fig. 7). The associated column densities are in the order of  $10^{15}~{\rm cm}^{-2}$  for C<sub>2</sub>H and  $4\times10^{14}~{\rm cm}^{-2}$  for C<sub>3</sub>H<sub>2</sub>. That is, between factors three and ten larger than what we found from the rotational diagrams for each species.

The difference between the observed column densities and those predicted by the homogeneous PDR models can arise from the unresolved clumpiness in the gas, which is not taken into account in the calculations based on our observations. Hence, the column densities estimated from observations should be considered lower limits of the actual column densities of the species. The slab depth dependent  $[C_2H/C_3H_2]$  abundance ratios are shown in Fig. 8 for the same models presented in Fig. 7. The  $C_2H$  molecule is about ten orders of magnitude more abundant over most of the slab's length for all the cases studied. How-



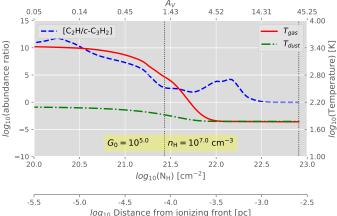


Fig. 8. The  $[C_2H/C_3H_2]$  abundance ratios from the PDR models. The left ordinate corresponds to the abundance ratio while the right ordinate corresponds to the gas and dust temperatures. Other labels are as in Fig. 7.

ever, the abundance ratio decreases to just about factor two in the lower density model ( $n_{\rm H}=10^6~{\rm cm}^{-3}$ ) toward the far edge of the slab. In the higher density model ( $n_{\rm H}=10^7~{\rm cm}^{-3}$ ) instead the abundance ratio turns around as the gas cools down and  $C_3H_2$  becomes about four times more abundant than  $C_2H$ . Gas temperatures reached at the far edge of the slab are about 45 K for the lower density model and about 60 K for the higher density model. Considering all the region of the slab where  $H_2$  is the most abundant species, the average gas temperatures are about 100 K and 120 K for the lower and higher density PDR models, respectively. These average temperatures are similar to the values (100–150 K) we (Tiwari et al. 2018) obtained for this region of M8.

Despite not considering surface grain chemistry or mechanisms about PAH destruction due to UV radiation, the PDR models lead to temperatures comparable to our estimates based on the observations after using the same density values found with the non-LTE radiative transfer models. This is in favor of the argument that gas-phase chemistry is able to roughly explain the abundance of small hydrocarbons in high-UV flux PDRs.

#### 5. Discussion

#### 5.1. Physical conditions probed by two velocity components

Two spectrally resolved velocity components are seen in the  $N=5\to 4$  transition of  $C_2H$  (Fig. 1) and are very prominent in all transitions of c- $C_3H_2$  (Fig. 2). These two components probe regions of different temperatures and densities. As mentioned before, the low velocity component (2–8 km s<sup>-1</sup>) is a part of the gas in the foreground veil and the high velocity component (8–15 km s<sup>-1</sup>) is a part of the gas close to Her 36 and the background molecular cloud. Owing to the prominent foreground veil feature in c- $C_3H_2$ , it seems to be a better probe of the warm PDR as compared to  $C_2H$ .

The rotational diagram analysis performed in Sect. 4.2, provides us with the column densities and abundances of the low and high velocity components of  $C_2H$  and c- $C_3H_2$ . Lower column densities and abundances are found in the foreground veil compared to the high column densities and abundances obtained in the gas close to Her 36 and in the background molecular cloud. As described in Sect. 4.3, the non-LTE RADEX modeling provides us with  $H_2$  volume density estimates. The low velocity component (corresponding to the foreground veil) probes the

high density gas in the range of  $5 \times 10^5$ – $5 \times 10^6$  cm<sup>-3</sup>. While, the high velocity component (corresponding to the gas close to Her 36 and in the background molecular cloud) probes both high and low density gas in the range of  $5 \times 10^4$ – $5 \times 10^6$  cm<sup>-3</sup>.

#### 5.2. Comparison with the Orion Bar PDR

The Orion Bar, an elongated structure in the Orion Nebula (M43), is the most-studied dense PDR (Tielens et al. 1993, Hollenbach & Tielens 1997 & Walmsley et al. 2000). In particular, it is an interesting source to study small hydrocarbon chemistry in ISM. Hogerheijde et al. (1995), Walmsley et al. (2000); and Andree-Labsch et al. (2017) described the geometry of the Orion Bar where the prominent O stars in the Trapezium illuminate the PDR, whose orientation changes from face-on to an edge-on relative to the line of sight and which appears to be located at the edge of the HII blister (Peng et al. 2012). Recent observational studies of small hydrocarbons toward this PDR have been reported by Cuadrado et al. (2015), who studied the chemistry and spatial distribution of C<sub>2</sub>H, C<sub>4</sub>H, c-C<sub>3</sub>H<sub>2</sub>, c-C<sub>3</sub>H and by Nagy et al. (2015), who constrained the physical conditions of the C<sub>2</sub>H (high transitions from  $N = 6 \rightarrow 5$  to  $10 \rightarrow 9$ ) emitting gas toward the Orion Bar.

In Table 5, we compared the  $C_2H$  and  $c\text{-}C_3H_2$  column densities toward M8 that we observe and obtain from modeling with those reported toward the Orion Bar by Cuadrado et al. (2015). We find the observed column densities to be similar in both PDRs, which was expected as we also found such similarities in the  $H_2$  volume density, in the kinetic temperature and in the CO and [C  $\Pi$ ] luminosities (Tiwari et al. 2018).

On the other hand, we found significant differences between the observed and the modeled column density of the  $C_3H_2$  molecule. In the case of Orion it is about one order of magnitude *lower* than estimated from the observations. In the case of M8 the modeled column density is between one and two orders of magnitude *larger* than estimated from observations, which is in line with the assumption that column densities we have determined should be considered lower limits. This suggests that there might be a significant difference between the results obtained with the Meudon PDR model used by Cuadrado et al. (2015) and our PDR model based on Meijerink & Spaans (2005). As shown in Appendix C.1, we ran our models for the Orion Bar with the same input parameters ( $n_{\rm H} = 4 \times 10^6~{\rm cm}^{-3}$  and  $G_0 = 1.17 \times 10^4$ )

Table 5. Column densities of C<sub>2</sub>H and c-C<sub>3</sub>H<sub>2</sub> in M8 and the Orion Bar

Species	Column densities $\log_{10}(N)$ (cm <sup>-2</sup> )						
	Obs	erveda	PDR model <sup>b</sup>				
	M8 Orion		M8	Orion			
$C_2H$	14.6	14.6	15	14.1-14.8			
$c-C_3H_2$	13.5	13.1	14.6-14.9	12.2-12.9			

<sup>&</sup>lt;sup>a</sup> Values for M8, calculated from Table 4 and for Orion Bar, obtained from Cuadrado et al. (2015, Table 7).

as used by Cuadrado et al. (2015, Fig. 17, right panel). We believe that the different chemical networks used in each model that lead to the formation and destruction of the C<sub>3</sub>H<sub>2</sub> molecule, are mainly responsible for their different column density predictions.

#### 6. Conclusions

In this paper, we report APEX and IRAM 30 m observations of the  $N=1\rightarrow 0, 3\rightarrow 2$  and  $5\rightarrow 4$  transitions of C<sub>2</sub>H and of the J =  $2 \rightarrow 1$ ,  $6 \rightarrow 5$ ,  $7 \rightarrow 6$  and  $8 \rightarrow 7$  transitions of c-C<sub>3</sub>H<sub>2</sub> toward M8. We presented the spectra of 18 observed hfs components of C<sub>2</sub>H and 5 observed transitions of ortho and para species of c-C<sub>3</sub>H<sub>2</sub> along with the velocity integrated intensity maps of the brightest  $N = 1 \rightarrow 0$ ,  $J = 3/2 \rightarrow 1/2$ ,  $F = 2 \rightarrow 1$  and  $N = 3 \rightarrow 2$ ,  $J = 7/2 \rightarrow 5/2$ ,  $F = 4 \rightarrow 3$  transitions of C<sub>2</sub>H.

As discussed in Sect. 4.2, we inferred column densities ranging from  $10^{12}$  to  $10^{14}$  cm<sup>-2</sup>.  $C_2H$  is more abundant than c- $C_3H_2$  with an abundance  $\sim 10^{-8}$ . The  $C_3H_2$  ortho/para ratio is calculated to be  $\sim 2.2$  for low velocity component (corresponding to the gas in the warm foreground veil) and 3.3 for high velocity component (corresponding to the gas near Her 36 and the background molecular cloud). We also expect c-C<sub>3</sub>H<sub>2</sub> to be a better probe than C<sub>2</sub>H for the warm PDR owing to its well defined low velocity component feature (seen in Fig. 2).

Using non-LTE RADEX modeling (Sect. 4.3), we constrained the H<sub>2</sub> volume densities of the hydrocarbon emitting gas to  $5 \times 10^4$  to  $5 \times 10^6$  cm<sup>-3</sup>. In Sect. 4.4, we compared the observed column densities with updated PDR models and they match the observed C<sub>2</sub>H column densities reasonably well (by a factor ~ 3) but predict higher values for c-C<sub>3</sub>H<sub>2</sub> (by a factor ~ 10–25). This discrepancy might arise from clumpy gas structure that we do not resolve with our observations. Therefore, the column densities derived from our data should be considered to be lower limits. The spatial distribution of PAH emission does not follow the C<sub>2</sub>H emission. This is consistent with PDR models, which do not require PAH fragmentation to explain the observed column densities of C<sub>2</sub>H and c-C<sub>3</sub>H<sub>2</sub> in M8.

#### References

Agúndez, M., Cernicharo, J., & Guélin, M. 2010, ApJ, 724, L133 Andree-Labsch, S., Ossenkopf-Okada, V., & Röllig, M. 2017, A&A, 598, A2 Arias, J. I., Barbá, R. H., Gamen, R. C., et al. 2010, ApJ, 710, L30 Arias, J. I., Barbá, R. H., Maíz Apellániz, J., Morrell, N. I., & Rubio, M. 2006, MNRAS, 366, 739

Benjamin, R. A., Churchwell, E., Babler, B. L., et al. 2003, PASP, 115, 953 Beuther, H., Semenov, D., Henning, T., & Linz, H. 2008, ApJ, 675, L33 Carter, M., Lazareff, B., Maier, D., et al. 2012, A&A, 538, A89

Chabot, M., Béroff, K., Gratier, P., Jallat, A., & Wakelam, V. 2013, ApJ, 771, 90 Chandra, S. & Kegel, W. H. 2000, A&AS, 142, 113 Cuadrado, S., Goicoechea, J. R., Pilleri, P., et al. 2015, A&A, 575, A82 Dahlstrom, J., York, D. G., Welty, D. E., et al. 2013, ApJ, 773, 41 Damiani, F., Bonito, R., Prisinzano, L., et al. 2017, A&A, 604, A135 Damiani, F., Flaccomio, E., Micela, G., et al. 2004, ApJ, 608, 781 Esteban, C., Peimbert, M., Torres-Peimbert, S., García-Rojas, J., & Rodríguez, M. 1999, ApJS, 120, 113 Gerin, M., Kaźmierczak, M., Jastrzebska, M., et al. 2011, A&A, 525, A116 Goldsmith, P. F. & Langer, W. D. 1999, ApJ, 517, 209 Goto, M., Stecklum, B., Linz, H., et al. 2006, ApJ, 649, 299 Griffin, M. J., Abergel, A., Abreu, A., et al. 2010, A&A, 518, L3 Güsten, R., Booth, R. S., Cesarsky, C., et al. 2006, in Proc. SPIE, Vol. 6267, Society of Photo-Optical Instrumentation Engineers (SPIE) Conference Series, 626714 Güver, T. & Özel, F. 2009, MNRAS, 400, 2050 Habing, H. J. 1969, Bull. Astron. Inst. Netherlands, 20, 177 Hogerheijde, M. R., Jansen, D. J., & van Dishoeck, E. F. 1995, A&A, 294, 792 Hollenbach, D. J. & Tielens, A. G. G. M. 1997, ARA&A, 35, 179 Le Page, V., Snow, T. P., & Bierbaum, V. M. 2003, ApJ, 584, 316 Lucas, R. & Liszt, H. S. 2000, A&A, 358, 1069 Matthews, H. E. & Irvine, W. M. 1985, ApJ, 298, L61 Meijerink, R. & Spaans, M. 2005, A&A, 436, 397 Montillaud, J., Joblin, C., & Toublanc, D. 2013, A&A, 552, A15 Nagy, Z., Ossenkopf, V., Van der Tak, F. F. S., et al. 2015, A&A, 578, A124 Oka, T., Welty, D. E., Johnson, S., et al. 2014, ApJ, 793, 68 Peng, T.-C., Wyrowski, F., Zapata, L. A., Güsten, R., & Menten, K. M. 2012, A&A, 538, A12 Pety, J., Teyssier, D., Fossé, D., et al. 2005, A&A, 435, 885 Pilbratt, G. L., Riedinger, J. R., Passvogel, T., et al. 2010, A&A, 518, L1 Pratap, P., Dickens, J. E., Snell, R. L., et al. 1997, ApJ, 486, 862 Rauw, G., Sana, H., Spano, M., et al. 2012, A&A, 542, A95 Sanchez-Bermudez, J., Alberdi, A., Schödel, R., et al. 2014, A&A, 572, L1 Schmidt, D. R. & Ziurys, L. M. 2017, ApJ, 850, 123 Schöier, F. L., van der Tak, F. F. S., van Dishoeck, E. F., & Black, J. H. 2005, A&A, 432, 369 Spezzano, S., Tamassia, F., Thorwirth, S., et al. 2012, ApJS, 200, 1 Spielfiedel, A., Feautrier, N., Najar, F., et al. 2012, MNRAS, 421, 1891 Stecklum, B., Henning, T., Eckart, A., Howell, R. R., & Hoare, M. G. 1995, ApJ, 445, L153 Teyssier, D., Fossé, D., Gerin, M., et al. 2004, A&A, 417, 135 Thaddeus, P., Gottlieb, C. A., Hjalmarson, A., et al. 1985, ApJ, 294, L49 Tielens, A. G. G. M. 2008, ARA&A, 46, 289 Tielens, A. G. G. M. & Hollenbach, D. 1985, ApJ, 291, 722 Tielens, A. G. G. M., Meixner, M. M., van der Werf, P. P., et al. 1993, Science, Tiwari, M., Menten, K. M., Wyrowski, F., et al. 2018, A&A, 615, A158 Tothill, N. F. H., Gagné, M., Stecklum, B., & Kenworthy, M. A. 2008, The Lagoon Nebula and its Vicinity, ed. B. Reipurth, 533 van der Tak, F. F. S., Black, J. H., Schöier, F. L., Jansen, D. J., & van Dishoeck, E. F. 2007, A&A, 468, 627 Walmsley, C. M., Natta, A., Oliva, E., & Testi, L. 2000, A&A, 364, 301 York, D. G., Dahlstrom, J., Welty, D. E., et al. 2014, in IAU Symposium, Vol.

Tucker, K. D., Kutner, M. L., & Thaddeus, P. 1974, ApJ, 193, L115

Woodward, C. E., Pipher, J. L., Helfer, H. L., et al. 1986, AJ, 91, 870 Woolf, N. J. 1961, PASP, 73, 206

297, The Diffuse Interstellar Bands, ed. J. Cami & N. L. J. Cox, 89-93 Young, E. T., Becklin, E. E., Marcum, P. M., et al. 2012, ApJ, 749, L17

<sup>&</sup>lt;sup>b</sup> Values for M8, obtained from the modeling results presented in Sect. 4.4 and for Orion Bar, obtained from Cuadrado et al. (2015, Table 7).

### Appendix A: Identified lines of hydrocarbons

**Table A.1.** Line intensities of the observed hfs transitions of  $C_2H$  line taken from CDMS.

Transition	Frequency	S <sub>ij</sub> <sup>a</sup>	$T_{mb}^{b}$	Relative	Intensities			
$\overline{(J,F)_{N=p+1} \to (J,F)_{N=p}}$	GHz		K	LTEc	Obs.d			
$C_2H N = 1 - 0$ with IRAM 30m/EMIR								
$(3/2,1) \to (1/2,1)$	87.284	0.17	0.16	0.042	0.055			
$(3/2,2) \to (1/2,1)$	87.316	1.67	1.10	0.416	0.392			
$(3/2,1) \rightarrow (1/2,0)$	87.328	0.83	0.57	0.207	0.204			
$(1/2,1) \to (1/2,1)$	87.401	0.83	0.58	0.208	0.208			
$(1/2,0) \rightarrow (1/2,1)$	87.407	0.33	0.25	0.083	0.088			
$(1/2,1) \rightarrow (1/2,0)$	87.446	0.17	0.15	0.042	0.052			
$\overline{C_2}$	H N = 3 - 2 v	with APE	EX/PI230	)				
$(7/2,3) \to (5/2,3)$	261.978	0.110	0.006	0.009	0.013			
$(7/2,4) \rightarrow (5/2,3)$	262.004	3.857	1.45	0.321	0.290			
$(7/2,3) \to (5/2,2)$	262.006	2.886	1.37	0.240	0.270			
$(5/2,3) \to (3/2,2)$	262.064	2.755	1.00	0.230	0.197			
$(5/2,2) \to (3/2,1)$	262.067	1.800	0.948	0.150	0.186			
$(5/2,2) \to (3/2,2)$	262.078	0.242	0.102	0.020	0.020			
$(5/2,3) \to (5/2,3)$	262.208	0.223	0.123	0.019	0.024			
$(5/2,2) \to (5/2,2)$	262.250	0.091	0.005	0.008	0.010			
$C_2H N = 5 - 4$ with APEX/FLASH <sup>+</sup>								
$(11/2,6) \rightarrow (9/2,5)$	436.661	5.910	0.8	0.298	0.296			
$(11/2,5) \rightarrow (9/2,4)$	436.662	4.921	0.7	0.248	0.259			
$(9/2,5) \to (7/2,4)$	436.723	4.837	0.665	0.245	0.246			
$(9/2,4) \to (7/2,3)$	436.724	3.890	0.535	0.196	0.198			

 $<sup>\</sup>overline{\ ^{a}}$  Theoretical line strengths.  $^{b}$  Observed main beam temperatures.  $^{c}$   $S_{ij}/\sum S_{ij},$  assuming optically thin transitions ( $\tau<1$ )  $^{d}$   $T_{mb_{ij}}/\sum T_{mb_{ij}}$ 

# Appendix B: Spatial distribution of [C I] and CO $J = 6 \rightarrow 5$ relative to C<sub>2</sub>H $N = 1 \rightarrow 0$

As shown in Fig. B.1, [C I] emission (in color) peaks close to Her 36 and has a bright extended emission toward the northwest of it. This extended emission is also traced by CO  $J=6 \rightarrow 5$  emission (white contours) as well as by  $C_2H N = 1 \rightarrow 0$  emission (black contours).

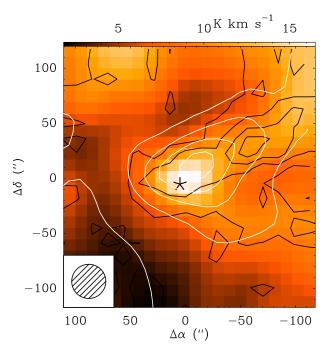


**Fig. B.1.** Colour map of velocity integrated intensity of the [C I] 609  $\mu$ m line overlaid with velocity integrated intensity map contours of C<sub>2</sub>H (in black) and CO  $J=6 \rightarrow 5$  (in white). Her 36 is the central position  $(\Delta\alpha=0, \Delta\delta=0)$  at R.A.(J2000) =  $18^h03^m40.3^s$  and Dec.(J2000) =  $-24^\circ22'43''$ , marked with an asterisk. For both C<sub>2</sub>H and CO  $J=6 \rightarrow 5$ , the contour levels are 10% to 100% in steps of 20% of the peak emission. All maps were convolved to the same resolution of 30".

# Appendix C: PDR modeling results for Orion Bar conditions

To investigate the different c-C<sub>3</sub>H<sub>2</sub> column density values obtained by our PDR models (Meijerink & Spaans 2005) for M8 and by the Meudon code for the Orion Bar, we ran our models using the same input parameters as Cuadrado et al. (2015, Fig. 17, right panel) for their high density clump ( $n_{\rm H}=4\times$  $10^6 \text{ cm}^{-3}$  and  $G_0 = 1.17 \times 10^4$ ). The modeling results are presented in Fig. C.1. Clearly our models do not produce the same results as the Meudon code (Cuadrado et al. 2015, Fig. 17, right panel). The differences in both models lie in the initial abundances of various species, in their evolution profiles and in the temperature profiles throughout the slab ( $A_{\nu} = 0$  to 10). Differences may arise due to distinct chemical networks used in both models. The Meudon code run by Cuadrado et al. (2015) uses a total of 130 species and 2800 gas-phase reactions. The Meijerink & Spaans (2005) model, on the other hand, uses a total of 309 species and 4453 gas-phase reactions. The different initial abundances of the neutral and ionized carbon at the edge (A<sub>v</sub> = 0) of our PDR model and that of the Meudon code may also contribute to the higher column density prediction of c-C<sub>3</sub>H<sub>2</sub>. Furthermore, it is worth mentioning that the Meudon code includes the updated state-to-state reactions of vibrationally excited  $H_2$  with  $[C \, \textsc{ii}]$ ,  $[O \, \textsc{i}]$ , OH (Agúndez et al. 2010). It also has upgraded the carbon-bearing species network and used the most recent branching ratios for ion-molecule, neutral-neutral, dissociative recombination, and charge exchange reactions for carbon chains and hydrocarbon species as described in Chabot et al. (2013). These updates are missing in our PDR models. The actual impact of these exchange reactions cannot be measured until the PDR model by Meijerink & Spaans (2005) is updated.

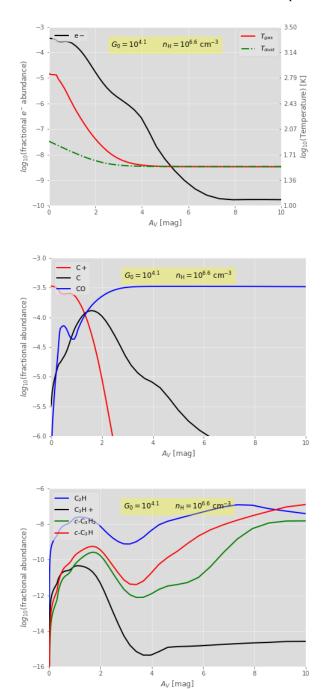


**Fig. C.1.** Results of our PDR modeling for a high density clump in the Orion Bar  $(n_{\rm H}=4\times10^6~{\rm cm^{-3}}$  and  $G_0=1.17\times10^4)$ . In all panels, the abscissa gives visual extinction. The top panel shows the dependence of the electron abundance (black solid line/ left ordinate), gas temperature (red solid line/ right ordinate) and dust temperature (red line, green dash-dot/ right ordinate). The middle panel plots the fractional abundances of ionized and neutral carbon and CO as red, black and blue lines, respectively. The bottom panel plots the fractional abundances of  $C_2H$ ,  $C_2H^+$ ,  $c\text{-}C_3H_2$  and  $c\text{-}C_3H$  as ionized and neutral carbon and CO as blue, black, green and red lines, respectively.